

A large accretion disk of extreme eccentricity in the TDE ASASSN-14li

R. Cao,¹ F.K. Liu,^{1,2*} Z.Q. Zhou,¹ S. Komossa,³ L.C. Ho^{2,1}

¹Department of Astronomy, School of Physics, Peking University, Beijing 100871, China

²Kavli Institute for Astronomy and Astrophysics, Peking University, Beijing 100871, China

³Max-Planck-Institut für Radioastronomie, Auf dem Hügel 69, 53121 Bonn, Germany

Accepted XXX. Received YYY; in original form ZZZ

ABSTRACT

In the canonical model for tidal disruption events (TDEs), the stellar debris circularizes quickly to form an accretion disk of size about twice the orbital pericenter of the star. Most TDEs and candidates discovered in the optical/UV have broad optical emission lines with complex and diverse profiles of puzzling origin. Liu et al. recently developed a relativistic elliptical disk model of constant eccentricity in radius for the broad optical emission lines of TDEs and well reproduced the double-peaked line profiles of the TDE candidate PTF09djl with a large and extremely eccentric accretion disk. In this paper, we show that the optical emission lines of the TDE ASASSN-14li with radically different profiles are well modelled with the relativistic elliptical disk model, too. The accretion disk of ASASSN-14li has an eccentricity 0.97 and semimajor axis of 847 times the Schwarzschild radius (r_S) of the black hole (BH). It forms as the consequence of tidal disruption of a star passing by a massive BH with orbital pericenter $25r_S$. The optical emission lines of ASASSN-14li are powered by an extended X-ray source of flat radial distribution overlapping the bulk of the accretion disk and the single-peaked asymmetric line profiles are mainly due to the orbital motion of the emitting matter within the disk plane of inclination about 26° and of pericenter orientation closely toward the observer. Our results suggest that modelling the complex line profiles is powerful in probing the structures of accretion disks and coronal X-ray sources in TDEs.

Key words: accretion disk — black hole physics — galaxies: active — line: profiles — quasars: supermassive black holes

1 INTRODUCTION

A star is tidally disrupted when it passes too close to a supermassive black hole (SMBH) in a galactic nucleus (Hills 1975; Rees 1988; Evans & Kochanek 1989; Lodato et al. 2009; Guillochon & Ramirez-Ruiz 2013; Hayasaki et al. 2013). About half the stellar debris after disruption becomes bound to the SMBH and returns to the orbital pericenter of the star. Hydrodynamic simulations of stellar tidal disruptions suggest that the returned bound stellar debris self-interacts because of relativistic apsidal precession of the debris orbits and circularizes on a timescale of a few times the return time of the most bound stellar debris to form an accretion disk (Rees 1988; Kochanek 1994; Hayasaki et al. 2013; Guillochon et al. 2014; Piran et al. 2015; Shiokawa et al. 2015; Bonnerot et al. 2016; Hayasaki & Loeb 2016; Sadowski et al. 2016). In the canonical scenario, the accretion disk is nearly circular and has size about twice the orbital pericenter of the star (but see Shiokawa et al. 2015). In this scenario, the light curves in the X-ray band are expected to follow the $t^{-5/3}$ fallback rate of stellar debris but

show some strong deviations in the optical/UV band. Stellar tidal disruption events (TDEs) discovered in the X-rays are consistent with these expectations, but those in the optical/UV band are not (Komossa & Bade 1999; Gezari et al. 2006; van Velzen et al. 2011; Komossa & Zensus 2016, for a recent review).

Most known TDEs and candidates discovered in the optical/UV have strong broad optical emission lines with complex, asymmetric, and diverse profiles (Komossa et al. 2008; Wang et al. 2012; Gezari et al. 2012; Arcavi et al. 2014; Holoien et al. 2014, 2016a,b; Cenko et al. 2016; French et al. 2016) and display large diversity in the relative strength of the He II and Balmer emission lines (Arcavi et al. 2014; French et al. 2016). Among them, some have abnormally strong He II emission lines while some have weak or absent He emission lines in the optical spectra (Komossa et al. 2008; Gezari et al. 2012; Wang et al. 2012; Arcavi et al. 2014; Gaskell & Rojas Lobos 2014; Gezari et al. 2015; French et al. 2016; Holoien et al. 2016a,b), whose nature and origin are not yet fully understood. Some recent models for the spectra of TDEs focus on the intensity ratios and widths of the optical emission lines (Gezari et al. 2012; Guillochon et al. 2014; Gaskell & Rojas Lobos 2014; Bogdanovic et al. 2014; Strubbe & Murray 2015; Kochanek

* E-mail: fkliu@pku.edu.cn (FKL)

2016; Krolik et al. 2016; Metzger & Stone 2016; Roth et al. 2016). Even tighter constraints on the origin of the emission lines may come from a more detailed investigation of the line profile shape and its variabilities.

Based on the hydrodynamic simulations for stellar tidal disruptions given in the literature, we recently developed a relativistic elliptical accretion disk model with constant eccentricity in radius for the broad optical emission lines of TDEs and well reproduced the complex substructures of the extremely broad double-peaked $H\alpha$ emission line of the TDE candidate PTF09djl (Liu et al. 2017). Liu et al. (2017) showed that the peculiar double-peaked profiles of the $H\alpha$ emission line of PTF09djl with one peak at the line rest wavelength and the other redshifted to about $3.5 \times 10^4 \text{ km s}^{-1}$ can be well modeled with an elliptical disk of a semimajor axis of $340r_S$ with r_S the BH Schwarzschild radius, large inclination 88° , and extreme constant eccentricity 0.966 in radius. A large elliptical accretion disk of constant eccentricity in radius suggests a fast accretion of matter and slow circularization of stellar debris, inconsistent with the canonical model for TDEs (Rees 1988) but well consistent with the physical arguments for efficient viscous stress (Svirski et al. 2017) and observational constraints on the disk viscous time of a very small fraction of the return time of the most bound stellar debris (Mockler et al. 2018).

In this paper, we model the profile of the broad $H\alpha$ emission line of the TDE ASASSN-14li with the relativistic elliptical disk model. The $H\alpha$ emission line of the TDE ASASSN-14li has a single-peaked profile radically different from the double-peaked profiles of the broad $H\alpha$ emission line of PTF09djl. We show that the complex and asymmetric substructures of the $H\alpha$ line profiles of the spectra of ASASSN-14li are also well reproduced with the elliptical relativistic disk model. The accretion disk of TDE ASASSN-14li has an extreme eccentricity 0.970 and large semimajor axis $847.0r_S$ and inclines with respect to the line of sight (LOS) by an angle about 26° . The single-peaked asymmetric line profiles are mainly due to the orbital motion of the emitting matter within the disk plane of small inclination and pericenter orientation closely toward the observer. The optical emission lines are powered by an extended X-ray source of flat radial distribution of radial extent about $1668.5r_S$, or the entire elliptical accretion disk. The enhanced He emission lines in the optical spectra and low disk inclination of ASASSN-14li are consistent with the scenario that the strong He emission lines are expected to form in an ionized optically thick accretion disk and the viewing angle effects of disk inclinations drive the diversity of the relative He emission lines in TDEs.

The paper is organized as follow. We analyze the spectra of ASASSN-14li in Section 2. The formation of accretion disk in TDEs is presented in Section 3.1, and the disk model for the broad emission lines is presented in Section 3.2. The disk modeling of the broad $H\alpha$ profiles is given in Section 3.3. In Section 4, we give the inferred parameters of the elliptical accretion disk. Implications of our results are discussed in Section 5.

2 THE SPECTRAL DATA OF ASASSN-14li

The TDE ASASSN-14li was discovered in the redshift $z = 0.0206$ galaxy PGC 043234 (VII Zw 211) on 2014 November 22, and 22 follow-up optical spectra were obtained between 2014 December 2 and 2016 April 4 (Holoien et al. 2016a; Brown et al. 2017). An optical spectrum of the host galaxy PGC 043234 is available from the Sloan Digital Sky Survey Data Release 9 (Ahn et al. 2012). The fluxes of the spectra were scaled so that the synthetic r -band magni-

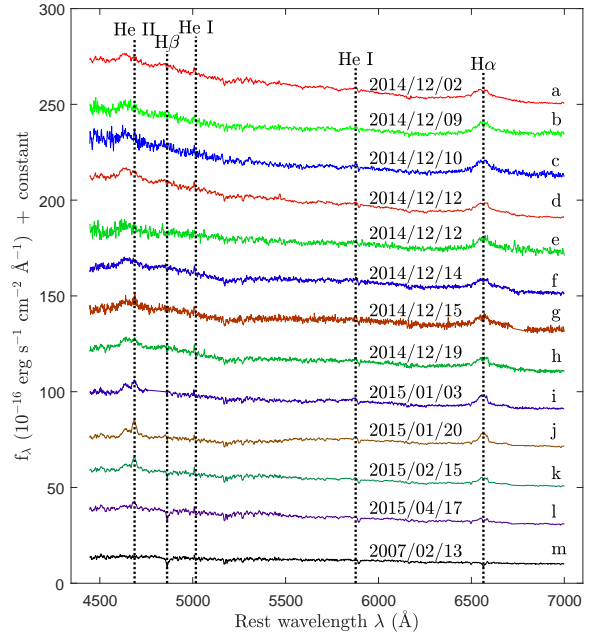


Figure 1. The optical spectra of ASASSN-14li (a-l), corrected for Galactic extinction, arranged in a time sequence from top to bottom and shifted vertically by arbitrary constants for clarity; the UT dates (year/month/day) of the observations are given above each spectrum. The spectrum of the host galaxy PGC 043234 is given at the bottom (m). Optical emission lines in the transient spectra, including Balmer lines, He I $\lambda 5016$, He I $\lambda 5876$ and He II $\lambda 4686$, are prominent and broad; they are identified with vertical dashed lines.

tudes from the spectra match the contemporaneous r -band photometry (Holoien et al. 2016a), although our results depend only on the line profiles and not on the absolute fluxes of the emission lines. We corrected the spectra for a Galactic extinction of $E(B - V) = 0.022$ mag (Cardelli et al. 1989; Schlafly & Finkbeiner 2011). We use stellar absorption lines to determine the systemic redshift of the host. The spectra of ASASSN-14li and the spectrum of host galaxy PGC 043234 are shown in Fig. 1. The Balmer, He I $\lambda 5016$, He I $\lambda 5876$, and He II $\lambda 4686$ lines except the possible He I $\lambda 6678$ are broad and prominent. In Fig. 1 and the rest of the paper, we do not include the three spectra from the MDM Observatory Hiltner 2.4 telescope obtained with the Ohio State Multi-Object Spectrograph with wavelength range 4200–6800 Å (Holoien et al. 2016a), because the wavelength limit is too close to that of redshifted $H\alpha$. Nor are the spectra of 2015 February 4, 2015 May 19, 2015 December 09, 2016 February 8, and 2016 April 4 included, whose signal-to-noise ratios are too low or the emission lines are too weak, with almost absent wings, to give a useful result.

To obtain a reliable measurement of the profiles of the broad emission lines for each epoch, we need to subtract the continuum, which contains contributions from a featureless component from the TDE and a component from the host galaxy starlight. The continuum of the TDE is modeled by fitting to several line-free regions of the TDE spectrum with a third-order polynomial¹, plus a scaled host spectrum. The host spectrum is scaled by matching the regions with strong stellar absorption features and without broad emission lines. Because the spectra of ASASSN-14li and the host galaxy were

¹ Different procedures of continuum fitting with higher order polynomials were tested, and produce the same line results.

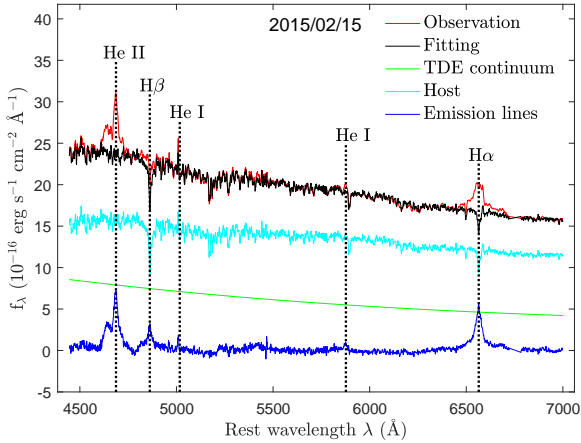


Figure 2. Sample spectral decomposition of one of the spectra of ASASSN-14li (2015 February 15). After correcting for Galactic extinction, the spectrum was fit with (1) a featureless TDE continuum, modeled with a third-order polynomial (green), and (2) host galaxy starlight (2007 February 13; light blue). The pure emission-line residual spectrum is shown in blue. Emission lines, including Balmer lines, He I $\lambda 5016$, He I $\lambda 5876$ and He II $\lambda 4686$, are identified with vertical dashed lines.

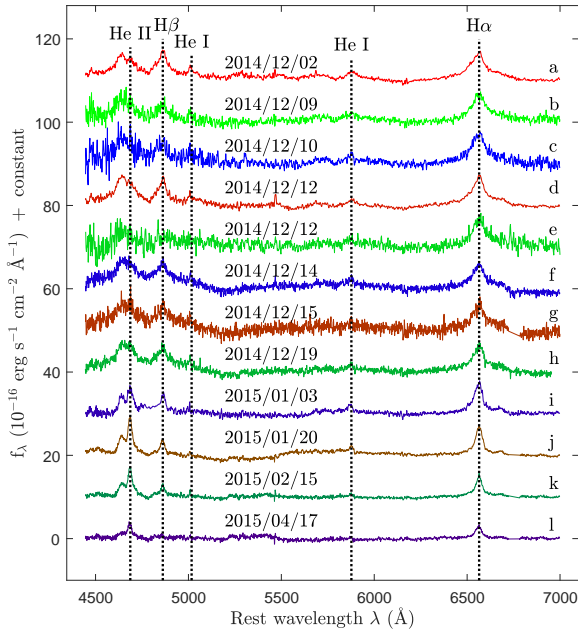


Figure 3. Emission-line spectra of ASASSN-14li (a-l). The spectra are obtained after Galactic extinction correction and subtraction of the continuum, globally modeled with a featureless TDE component and host galaxy starlight component (see Fig. 2). They are arranged in a time sequence from top to bottom, and shifted vertically by arbitrary constants for clarity; the UT dates (year/month/day) of the observations are given above each spectrum. Broad emission lines are identified with vertical dashed lines.

obtained using several telescopes with different spectral resolutions, we convolve all the spectra to match the lowest resolution of the spectra, $R \sim 8 \text{ \AA}$. Fig. 2 illustrates our spectral decomposition procedure for one of the spectra.

Fig. 3 gives the 12 emission-line spectra of ASASSN-14li after continuum and host galaxy starlight subtraction. $H\alpha$ is strong and broad, with full width at half maximum (FWHM) between 1700–4500 km s^{-1} at all epochs. Other broad Balmer lines and He I $\lambda 5016$,

He I $\lambda 5876$, and He II $\lambda 4686$ are also present, as initially reported by [Holoien et al. \(2016a\)](#). $H\alpha$ is the strongest and least blended feature in the spectrum, and the continuum is well-defined and relatively flat near $H\alpha$, minimizing uncertainties due to continuum subtraction. The other emission lines are blended with neighboring features and are more sensitive to the details of continuum modeling. Therefore, we base our analysis and conclusions on the results of modeling the asymmetric and complex profiles of the $H\alpha$ emission line.

3 MODELING THE BROAD EMISSION LINES OF ASASSN-14li

[Liu et al. \(2017\)](#) recently set up a relativistic elliptical disk model for the broad optical emission lines of TDEs. In this section, we present the disk model in some more detail and apply it to model the spectra of ASASSN-14li.

3.1 The accretion disk in TDEs

A star is tidally disrupted by a SMBH when its orbital pericenter r_p is less than the tidal disruption radius

$$r_t = R_* (M_{\text{BH}}/M_*)^{1/3} \approx 23.54 r_* m_*^{-1/3} M_6^{-2/3} r_S, \quad (1)$$

where $R_* = r_* R_\odot$ and $M_* = m_* M_\odot$ are, respectively, the star's radius and mass, and $M_{\text{BH}} = 10^6 M_\odot$ is the mass of the BH. When the bound stellar debris stream returns to the pericenter, it is compressed and a nozzle shock forms at pericenter. The hydrodynamic simulations of stellar tidal disruption indicate that the nozzle shock at the pericenter is weak and the stellar debris stream is circularized due to the interaction of the post-pericenter outflowing and newly inflowing streams because of relativistic apsidal precession ([Evans & Kochanek 1989](#); [Kochanek 1994](#); [Hayasaki et al. 2013](#); [Dai et al. 2015](#); [Shiokawa et al. 2015](#); [Piran et al. 2015](#); [Bonnerot et al. 2016](#); [Hayasaki & Loeb 2016](#)). The orbit of the most-bound stellar debris precesses by the instantaneous de Sitter precession angle

$$\Omega \approx \frac{6\pi G M_{\text{BH}}}{c^2 a_{\text{mb}} (1 - e_{\text{mb}}^2)} \approx \frac{6\pi G M_{\text{BH}}}{c^2 r_p (1 + e_{\text{mb}})} \approx \frac{3\pi r_S}{2 r_p} = \frac{3\pi}{2} \frac{1}{x_p} \quad (2)$$

with $x_p = r_p/r_S$, where $e_{\text{mb}} = 1 - \delta$ with $\delta \approx 8.49 \times 10^{-4} r_*^{-1} m_*^{2/3} M_6^{1/3} x_p$ is the eccentricity of the most-bound stellar debris. The orbital precession of the bound stellar debris leads to the interaction of the outflowing and inflowing streams at location ([Dai et al. 2015](#))

$$r_{\text{cr}} \approx \frac{(1 + e_{\text{mb}}) r_p}{1 - e_{\text{mb}} \cos(\Omega/2)} \approx \frac{2 x_p r_S}{\delta + 2 \sin^2(\Omega/4)}. \quad (3)$$

The location of the self-interaction determines the orientation and size of the elliptical accretion disc.

Provided that the inflowing and outflowing streams have similar mass and the collision is completely inelastic, the formed elliptical disk has a semimajor axis ([Dai et al. 2015](#))

$$a_d \approx \frac{r_{\text{cr}}}{2 \sin^2(\theta_c/2)} \frac{1}{1 + (r_{\text{cr}}/2a_{\text{mb}}) \cot^2(\theta_c/2)}, \quad (4)$$

where $a_{\text{mb}} \approx r_t^2/2R_*$ is the orbital semimajor axis of the most-bound stellar debris nearly independent of the orbital penetration factor $\beta = r_t/r_p$ ([Guillochon & Ramirez-Ruiz 2013](#); [Hayasaki et al.](#)

2013) and θ_c is the intersection angle of the outgoing stream with the incoming stream, given by

$$\cos(\theta_c) = \frac{1 - 2 \cos(\Omega/2)e_{\text{mb}} + \cos(\Omega)e_{\text{mb}}^2}{1 - 2 \cos(\Omega/2)e_{\text{mb}} + e_{\text{mb}}^2}, \quad (5)$$

which gives

$$\sin(\theta_c/2) = \frac{2 \sin(\Omega/4) \cos(\Omega/4)}{\sqrt{\delta^2 + 4 \sin^2(\Omega/4) - 4\delta \sin^2(\Omega/4)}} \simeq \cos(\Omega/4) \quad (6)$$

(Liu et al. 2017). From Equation (4) together with Equations (3) and (6), we have

$$a_d \simeq \frac{2x_p}{2\delta + \sin^2(\Omega/2)} r_S \quad (7)$$

(Liu et al. 2017). For low-mass main sequence stars ($0.1 \leq m_* \leq 1$) with $r_* \simeq m_*^{1-\zeta}$ and $\zeta \simeq 0.2$ (Kippenhahn & Weigert 1994), we have $\delta \simeq 8.49 \times 10^{-4} m_*^{-2/15} M_6^{1/3} x_p$.

In a completely inelastic collision, no angular momentum transfers and redistributes between the outgoing and incoming streams. The shocked stream has specific angular momentum $j_{\text{mb}} \simeq \sqrt{(1 + e_{\text{mb}})r_p G M_{\text{BH}}}$. The conservation of angular momentum of the shocked stream gives an eccentricity of the debris accretion disk

$$e_d \simeq \left[1 - \frac{(1 + e_{\text{mb}})r_p}{a_d} \right]^{1/2} \simeq \left[\cos^2 \left(\frac{\Omega}{2} \right) - 2\delta \right]^{1/2}. \quad (8)$$

3.2 A disk model for the broad emission lines

Following Liu et al. (2017), we suggest that the broad optical emission lines of TDEs are generated in the elliptical accretion disk presented in Sec. 3.1. It is not very clear how the optical emission lines are excited in the accretion disk. The observations of TDE candidates in the archive of *Swift* Burst Alert Telescope (BAT) show that there is tentative evidence that hard X-rays may be common in unbeamed tidal disruption events (Hryniewicz & Walter 2016). A significant fraction of TDEs has been identified and detected in X-rays (see Komossa 2015, for a recent review). The accretion disk in TDEs is ionized and irradiated by the coronal X-ray source. Because the poloidal magnetic field lines are anchored to the ionized accretion disk and the coronal X-ray source is powered by the reconnection of the field lines, the coronal materials would move nearly radially and become radially extended.

An ionized accretion disk irradiated by X-ray sources could produce strong optical emission lines only if the ionization parameter is low to intermediate (García et al. 2013). To approximate the reflection optical line emissivity of the accretion disk irradiated by an extended X-ray source, we adopt the broken power law in radius r (Wilkins & Fabian 2012; Gonzalez et al. 2017)

$$I_{\nu_e} = \begin{cases} \frac{\epsilon_0 c}{2(2\pi)^{3/2} \sigma} \left(\frac{\xi}{\xi_{\text{br}}} \right)^{-\alpha_1} \exp \left[-\frac{(\nu_e - \nu_0)^2 c^2}{2\nu_0^2 \sigma^2} \right] & \text{for } \xi \leq \xi_{\text{br}} \\ \frac{\epsilon_0 c}{2(2\pi)^{3/2} \sigma} \left(\frac{\xi}{\xi_{\text{br}}} \right)^{-\alpha_2} \exp \left[-\frac{(\nu_e - \nu_0)^2 c^2}{2\nu_0^2 \sigma^2} \right] & \text{for } \xi > \xi_{\text{br}} \end{cases} \quad (9)$$

with $\xi = r/r_S$ and $\xi_{\text{br}} = r_{\text{br}}/r_S$ with r_{br} the radial extent of extended X-ray source, where ν_e is the frequency in the frame of the emitter, ϵ_0 is a constant to be fitted, c is the speed of light, ν_0 is the rest frequency of the emission line, and σ is a velocity dispersion of the local Gaussian line broadening because of thermal and turbulent motions. In Equation (9), the emissivity power index α_2 is fixed with the typical $\alpha_2 \simeq 3$, and α_1 depends on the radial distribution of

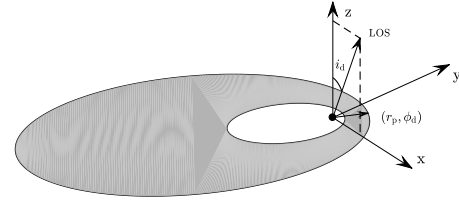


Figure 4. General scheme illustrating the geometry and coordinate system used in the profile calculations. The z -axis is along the rotation axis of the accretion disk, and the accretion disk lies within the xy -plane. The line-of-sight of the observer at infinity is in the xz -plane and makes an inclination angle i_d to the z -axis.

X-ray sources and can be used to probe the geometry of the coronal X-ray source (Wilkins & Fabian 2012; Gonzalez et al. 2017).

The specific flux at frequency ν received by the observer at infinity is given by

$$f_\nu = \frac{r_S^2 \cos i_d}{d^2} \int \int \xi d\xi d\phi I_{\nu_e} D^3(\xi, \phi) \psi(\xi, \phi) \quad (10)$$

(Eracleous et al. 1995; De Falco et al. 2016), where ϕ is the azimuthal angle around the disk with respect to the projected observer's LOS in the disk plane, function $\psi(\xi, \phi)$ describes the effects of curved trajectories of light rays (Beloborodov 2002; De Falco et al. 2016); $D(\xi, \phi) \equiv \nu/\nu_e$, and d and i_d are, respectively, the Doppler factor, luminosity distance to the source, and disk inclination angle with respect to the LOS. The schematic geometry and coordinate systems are shown in Fig. 4.

The Doppler factor $D(\xi, \phi)$ describes the effects of gravity and the motion of the emitting particles on the energies of the emitted photons

$$D = \frac{(1 - 1/\xi)^{1/2}}{\gamma} \left\{ 1 - \frac{\beta_r [1 - (b/r)^2 (1 - 1/\xi)]^{1/2}}{1 - 1/\xi} + \frac{\beta_\phi (b/r) \sin i_d \sin \phi}{(1 - \sin^2 i_d \cos^2 \phi)^{1/2}} \right\}^{-1} \quad (11)$$

(Eracleous et al. 1995), where $\beta_r = (dr/dt)/c$ and $\beta_\phi = r(d\phi/dt)/c$ are, respectively, the radial and azimuthal velocities of the emitting particles in the source frame, and γ is the Lorentz factor $\gamma = [1 - \beta_r^2 (1 - 1/\xi)^{-2} - \beta_\phi^2 (1 - 1/\xi)^{-1}]^{-1/2}$. The ratio (b/r) of the impact parameter at infinity and the radius describes how rays emitted from the debris are mapped to points in the image at infinity (Eracleous et al. 1995; Beloborodov 2002; De Falco et al. 2016).

The generalized Newtonian potential in the low-energy limit (Tejeda & Rosswog 2013) is adopted to describe the motion of particles in the disk plane, because it can reproduce exactly the trajectories of particles in Schwarzschild space-time and the radial dependences of the specific binding energy and angular momentum of the elliptical orbits. With the generalized Newtonian potential, the radial and azimuthal velocities of the emitting particles in the source frame are, respectively,

$$\beta_r \simeq \left(1 - \frac{1}{\xi} \right) \sqrt{2 \frac{E_G}{c^2} + \frac{1}{\xi} - \frac{l_G^2}{r_S^2 c^2 \xi^2} \left(1 - \frac{1}{\xi} \right)}, \quad (12)$$

$$\beta_\phi \simeq \frac{l_G}{r_S c} \frac{\xi - 1}{\xi^2}, \quad (13)$$

where l_G and E_G are, respectively, the orbital specific angular momentum and energy (Tejeda & Rosswog 2013). For an elliptical

orbit with semimajor axis a and eccentricity e , l_G and E_G are fixed, respectively,

$$\frac{l_G}{r_S c} = \frac{(1 - e^2)x_a}{\sqrt{2(1 - e^2)x_a - 3 - e^2}}, \quad (14)$$

$$\frac{E_G}{c^2} = -\frac{1}{2} \frac{x_a(1 - e^2) - 2}{x_a [2x_a(1 - e^2) - 3 - e^2]}, \quad (15)$$

where $x_a = a/r_S$.

It is unclear whether the stream within the accretion disk gets circularized (Bonnerot et al. 2017) or remains highly eccentric (Svirski et al. 2017) at accretion onto the BH. Following Liu et al. (2017), we assume that the eccentric disk consists of nested elliptical annuli with a single eccentricity, which does not vary with semi-major axis², or that the disk viscous time is much smaller than the circularization time of stellar debris. The particles in a given elliptical annulus of pericenter orientation ϕ_d have trajectories

$$r = \frac{a(1 - e^2)}{1 + e \cos(\phi - \phi_d)}. \quad (16)$$

The disk pericenter orientates toward the observer at $\phi_d = 0^\circ$.

3.3 Fitting the H α profiles of ASASSN-14li

To fit the H α line profiles, we first calculate a set of the model line profiles for the emission-line region between the inner radius ξ_1 with $2 \leq \xi_1 \leq 70$ and the outer radius ξ_2 with $\xi_2 = (1 + e_d)a_d/r_S$. The elliptical accretion disk has an inner edge $2r_S$, because the accretion disk is extremely eccentric ($e_d \approx 0.970$; see Section 4) and the disk fluid elements with nearly parabolic orbits passing through the marginal bound orbit $2r_S$ fall freely on to the BH (Abramowicz et al. 1978). The disk semimajor axis a_d/r_S (and thus the disk outer edge) and eccentricity e_d are computed with Equations (7) and (8) for the star's orbital pericenter x_p for $1 \leq x_p \leq 50$. In modeling the line profiles, the BH mass is required only in the calculation of the disk semimajor axis and eccentricity through the small quantity δ in Equations (7) and (8). We do not estimate the BH mass by modeling the line profiles and adopted the BH mass $\lg(M_{\text{BH}}/M_\odot) = 6.23^{+0.39}_{-0.40}$ obtained with the $M_{\text{BH}} - \sigma_*$ correlation of the host bulge and central BH mass (Wevers et al. 2017), because the model line profiles are mainly determined by both the kinematic Doppler and gravitational lensing effects, which are functions of dimensionless radius ξ instead of the dimensional radius r (c.f. Equations 11 and 13). Having the BH mass as a free parameter would improve fits little and the estimate of BH mass has much larger uncertainties than that obtained from the $M_{\text{BH}} - \sigma_*$ relation.

The model line profiles are also computed for the parameter space, $0 \leq i_d \leq \pi$, $0 \leq \phi_d < 2\pi$, $\xi_{\text{br}} \leq \xi_2$, $5 \times 10^{-2} \times \text{FWHM} \leq \sigma \leq (2/3) \times \text{FWHM}$ and $0 \leq \alpha_1 \leq 3$. The observed H α line profiles of the 12 spectra are jointly fitted with shared periape x_p , inner radius ξ_1 , broken radius ξ_{br} , emissivity power-law index α_1 , and velocity dispersion σ with the least-square method (χ^2).

4 RESULTS

Fig. 5 shows the best-fit models of the 12 H α spectra and the reduced χ^2 . The reduced χ^2 is calculated with respect to the averaged noise

² Eccentricity with a power-law distribution in semimajor axis improve the fit little.

level over the closest regions of the emission lines after subtraction of the spectral features. Table 1 gives the best-fit values of the model parameters and their associated uncertainties at 90% confidence level. We calculated the uncertainties of the fitting parameters at 90% confidence level with the Markov Chain Monte Carlo (MCMC) method (Liu et al. 2017)

The results indicate that the broad complex and asymmetric emission-line profiles of the 12 H α spectra of TDE ASASSN-14li can be well fitted with a relativistic elliptical accretion disk model. The elliptical accretion disk has an extreme eccentricity $e_d \approx 0.9700^{+0.0002}_{-0.0013}$ and large semimajor axis $a_d \approx 847.0^{+23.3}_{-5.3} r_S$ (or apogee $1668.5 r_S$). The asymmetric and complex substructures of the line profiles are mainly due to the elliptical motion of the line-emitting matter within the disk plane with low inclination $i_d \sim 26^\circ$ and pericenter orientation $\phi_d \approx 2.7^\circ$, closely toward the observer. The elliptical accretion disk forms following the tidal disruption of a star with orbital pericenter $r_p \approx 25.33^{+1.82}_{-0.36} r_S$, passing by a BH of mass $M_{\text{BH}} \approx 10^6 M_\odot$ with penetration factor $\beta = r_t/r_p \approx 0.93 m_*^{-\zeta+2/3} M_6^{-2/3}$.

Our results show that the broad optical emission lines originate from the regions of the elliptical accretion disk from about $9r_S$ to the disk apogee $1668.5 r_S$ and is locally broadened with Gaussian velocity dispersion $\sigma \approx 279 \text{ km s}^{-1}$, about 17 times smaller than the local broadening of the H α line in the TDE candidate PTF09djl (Liu et al. 2017). The elliptical accretion disk is overlapped by an extended hot corona of radial extent $r_{\text{br}} \approx 1668.5 r_S$, or the entire disk radial extent. The disk is illuminated by the extended coronal X-ray source, and the line emissivity of disk reflection spectra is practically a single power-law in radius with index $\alpha_1 \approx -0.049^{+0.035}_{-0.032}$ for the entire disk region covered by the corona. A power-law index $\alpha_1 \approx 0$ is expected with an extended illuminating coronal X-ray source of flat radial distribution (Wilkins & Fabian 2012; Gonzalez et al. 2017).

Fig. 6 gives for comparison the evolution of the best-fit line emissivity constant ϵ_0 over time and the X-ray flux at 0.3-10 keV. The data of the *Swift* X-ray flux at 0.3-10 keV for the period of the observations of the 12 optical spectra are taken from Miller et al. (2015). The evolution of the X-ray flux is well fitted by a power-law $\propto t^{-1.74}$ and ϵ_0 is scaled by a constant $1.08 \times 10^{-40} \text{ sr } \text{\AA}$ to match the X-ray observations. Fig. 6 shows that the line emissivity constant ϵ_0 roughly follows the X-ray flux at 0.3-10 keV, implying a common energy source of the optical emission lines and the X-ray emission.

Fig. 7 gives the disk pericenter position and inclination angles as a function of the observational time. The disk pericenter position angle ϕ_d is nearly constant with $\phi_d \approx 2.7^\circ$ except that of the last spectra with $\phi_d \approx 20^\circ$, but the disk inclination decreases from about 38° at early epochs to 14° about 146 days after discovery. The changes in the line profiles are mainly due to the variations of the disk inclination. Because the orientation of the disk semimajor axis is determined by the location of the intersection of the outflowing and inflowing streams, a constant disk semimajor axis would imply an invariant orientation of the disk semimajor. However, the precession of elliptical disk would lead to an associated variation of the disk azimuthal angle. Fig. 7 shows that the observations of the disk inclination i_d and pericenter azimuthal angles ϕ_d are consistent with the precession of the elliptical accretion disk with precession period $T_{\text{LS}} \approx 954$ days. The $\phi_d - i_d$ diagram in Fig. 8 shows that the relationship of the disk azimuthal angle ϕ_d and inclination i_d is consistent with the expectation of the disk precession. The elliptical accretion disk precesses due to the Lense-Thirring effect because of the misalignment of the disk rotation axis and BH spin by an angle about 23.7° . The BH spin axis inclines with respect to the LOS

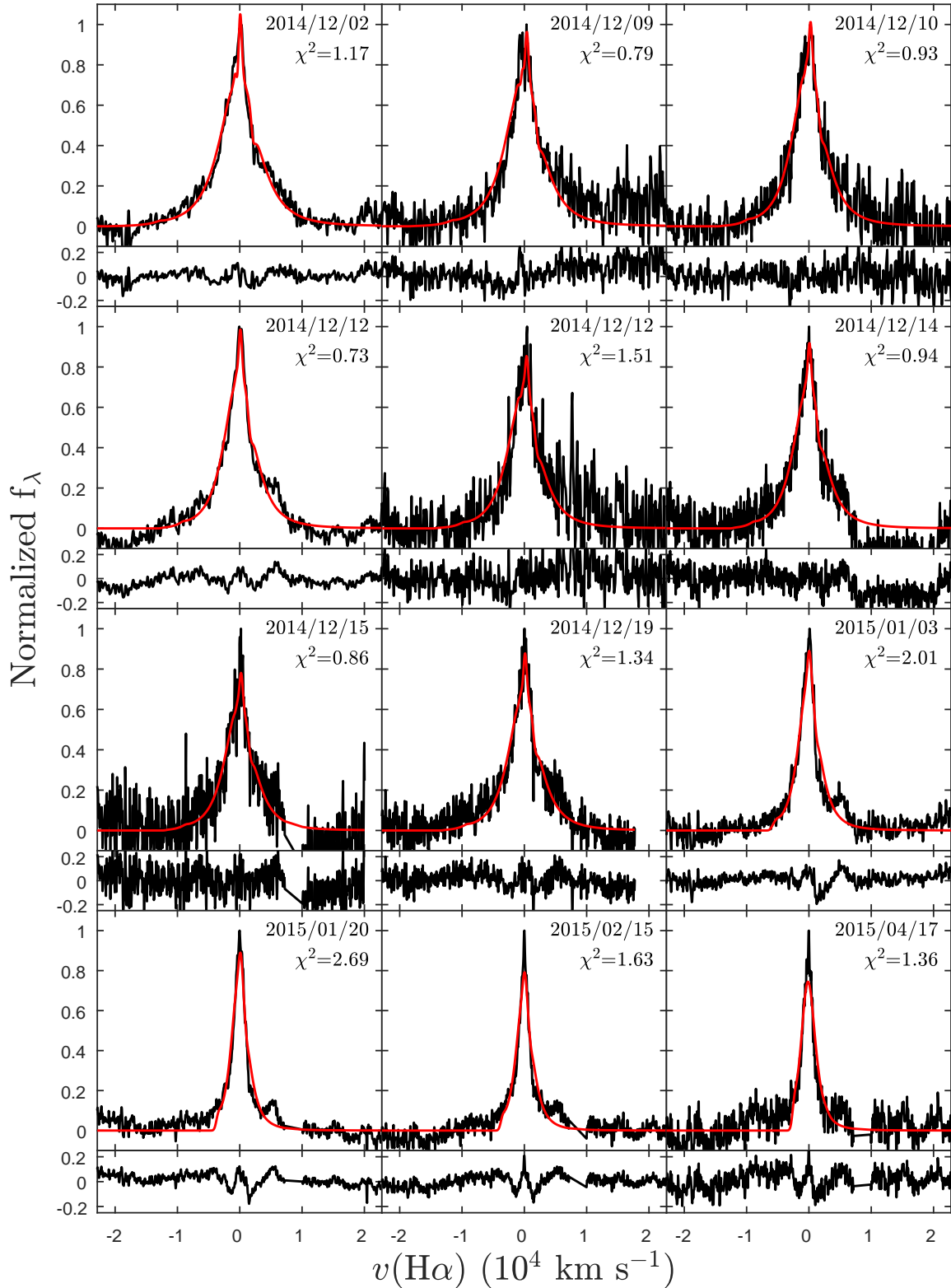


Figure 5. Normalized velocity profiles of H α and fits of the model spectra for different epochs. The UT date (year/month/day) is given at the top right of each panel. The observed profiles (black) are complex and asymmetric but are well reproduced with the relativistic elliptical disk model (red solid). The residuals of the spectra, after subtraction of the fit, are given at the bottom of each panel. The reduced χ^2 of the best fit is given at the top right of each panel.

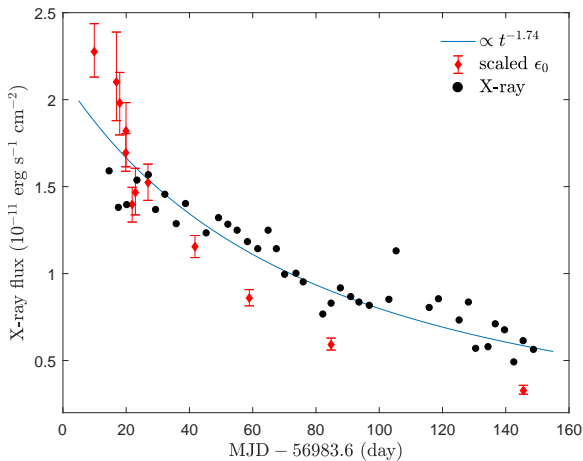


Figure 6. Evolution of the line emissivity constant ϵ_0 (diamonds) over time, starting at discovery (MJD = 56983.6 days). The filled circles are the 0.3–10 keV X-ray observations (Miller et al. 2015). The solid line gives a power-law fit of the X-ray flux. The line emissivity constant ϵ_0 is scaled with a constant 1.08×10^{-40} sr \AA and closely follows the X-rays at 0.3–10 keV, implying that the optical emission lines in TDEs are powered by the X-ray source.

by about 33.8° . Because the spectral observational campaign lasted only about 14% of the disk precession period T_{TS} , the present observations cannot give useful constraints on the parameters of disk precession, and much more spectral observations of high resolutions and signal-to-noise ratios are needed.

5 DISCUSSION AND CONCLUSION

We have analyzed a set of 12 optical spectra of the TDE ASASSN-14li, after careful treatment of the TDE featureless continuum and host galaxy starlight. We have successfully modelled the complex, asymmetric and single-peaked substructures of the broad $H\alpha$ emission line with a relativistic elliptical accretion disk model, although the profiles of the optical emission lines of ASASSN-14li are radically different from those of the double-peaked broad $H\alpha$ line of the TDE candidate PTF09djl (Liu et al. 2017). The results show that the TDE ASASSN-14li is powered by the tidal disruption of a star, passing by a BH of mass $M_{\text{BH}} \approx 10^{6.23} M_\odot$ with an orbital pericenter $r_p \approx 25.33 r_S$ or penetration factor $\beta \approx 0.93 m_*^{-\zeta+2/3} M_6^{-2/3}$. The returned bound stellar debris forms an elliptical accretion disk of a semimajor $a_d \approx 847.0 r_S$ and eccentricity $e_d \approx 0.970$. The elliptical accretion disk is irradiated by an extended coronal X-ray source with radial size of the total radial extent of the elliptical accretion disk. The coronal X-ray source has a flat radial distribution with a power-law of index $\alpha_1 \approx -0.049$. The debris accretion disk of ASASSN-14li has a nearly constant pericenter azimuthal position angle with $\phi_d \approx 2.7^\circ$ for most of the spectral observational time except that for the last spectral observation and decreasing inclination from $i_d \approx 38^\circ$ at early epoch to 14° at the last spectral observation.

The pericenter azimuthal position angle $\phi_d \sim 2.7^\circ$ suggests that the major axis of the elliptical accretion disk of ASASSN-14li nearly points toward the observer. The major axis of the elliptical accretion disk of the TDE candidate PTF09djl has a large disk pericenter position angle $\phi_d \approx 72^\circ$ (Liu et al. 2017). The orientations of the major axis of elliptical accretion disk in the two TDEs have a relative position angle $\Delta\phi_d \approx 69^\circ$ and are consistent with a roughly uniform distribution of ϕ_d between 0° and 360° or of $\Delta\phi_d$ be-

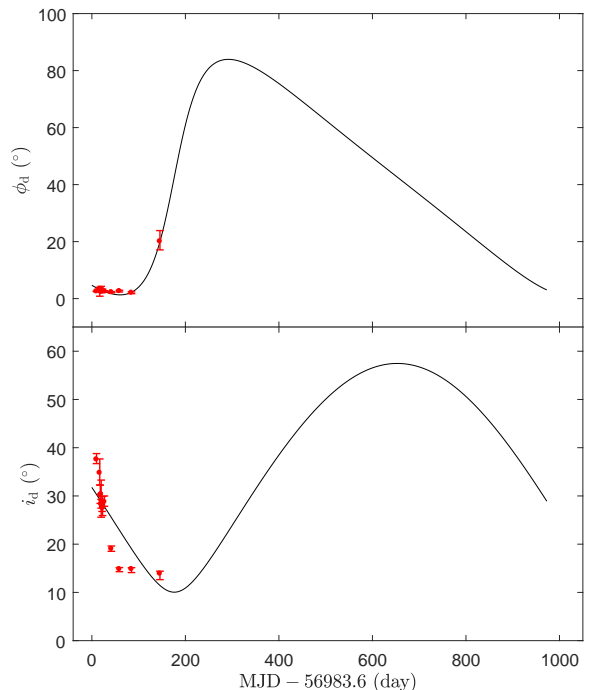


Figure 7. Disk periastron azimuthal angle ϕ_d (upper) and inclination i_d (lower) versus observational time, starting at discovery (MJD = 56983.6 days). The azimuthal angle is nearly constant for most time of the spectral observations and the inclination decreases with time, which are consistent with the precession of an elliptical accretion disk (solid) because of the Lense-Thirring effect with precession period $T_{\text{LS}} \approx 953.7$ days. The associated uncertainties at 90% confidence level calculated with MCMC are plotted.

tween 0° and 90° . We will check the conclusion by modeling the broad optical emission lines for a larger sample of TDEs.

The orientations of the elliptical accretion disk of the two TDEs are very different with respect to the observer and the profiles of optical emission lines strongly depend on the position angle ϕ_d for extremely eccentric disks. The profiles of the optical emission lines of the TDEs ASASSN-14li and PTF09djl are significantly different, being moderately broad and single-peaked for the former and extremely broad and double-peaked for the latter. For a power-law disk emissivity $I_{\nu_e} \sim \xi^{-\alpha}$, the line flux from the disk region at radius r is about $f_\nu \sim \xi^{2-\alpha}$. For a lamppost or compact illuminating X-ray source of power-law index $\alpha \sim 3$, as for PTF09djl (Liu et al. 2017), the line flux is mainly from the disk region at small radius ξ and would be significantly Doppler shifted by the large velocity of emitting particles. The optical lines may have double-peaked and Doppler-shifted profiles for moderate to large disk inclination, depending on the disk pericenter orientations ϕ_d . In contrast, for an extended flat corona with power-law index $\alpha \approx -0.049$, as for ASASSN-14li, the line emission is dominated by the flux from the disk surface at large radius ξ , where the kinematic velocity of the emitting particles is relatively small and the Doppler effect is insignificant. It would be expected that the optical emission lines are single-peaked with broad and asymmetric wings and the peak of line profiles may be low to moderately Doppler-shifted, depending on the disk pericenter orientation ϕ_d and inclination i_d . The observation that the optical emission lines in most optical/UV TDEs have asymmetric and single-peaked profiles may suggest that the optical emission lines in the TDEs are powered by an extended X-ray source with power-law index $\alpha \lesssim 2$.

Table 1. Best-fitting disk parameters and associated uncertainties for the broad H α emission line.

Date	r_p (r_S)	ϕ_d ($^\circ$)	i_d ($^\circ$)	a_d (r_S)	e_d	r_1 (r_S)	r_{br} (r_S)	α_1	σ (km s^{-1})	ϵ_0
2014/12/02	$25.33^{+1.82}_{-0.36}$	$2.5^{+0.1}_{-0.1}$	$37.6^{+1.2}_{-0.9}$	$847.0^{+23.3}_{-5.3}$	$0.9700^{+0.0002}_{-0.0013}$	$8.96^{+1.82}_{-2.12}$	$1668.5^{+44.8}_{-10.2}$	$-0.049^{+0.035}_{-0.032}$	279^{+11}_{-10}	$21.1^{+1.5}_{-1.4}$
2014/12/09	$25.33^{+1.82}_{-0.36}$	$3.4^{+0.6}_{-2.5}$	$34.8^{+2.9}_{-2.7}$	$847.0^{+23.3}_{-5.3}$	$0.9700^{+0.0002}_{-0.0013}$	$8.96^{+1.82}_{-2.12}$	$1668.5^{+44.8}_{-10.2}$	$-0.049^{+0.035}_{-0.032}$	279^{+11}_{-10}	$19.5^{+2.7}_{-1.6}$
2014/12/10	$25.33^{+1.82}_{-0.36}$	$3.0^{+0.3}_{-0.3}$	$30.1^{+2.1}_{-1.7}$	$847.0^{+23.3}_{-5.3}$	$0.9700^{+0.0002}_{-0.0013}$	$8.96^{+1.82}_{-2.12}$	$1668.5^{+44.8}_{-10.2}$	$-0.049^{+0.035}_{-0.032}$	279^{+11}_{-10}	$18.4^{+1.6}_{-1.7}$
2014/12/12	$25.33^{+1.82}_{-0.36}$	$2.5^{+0.2}_{-0.2}$	$28.3^{+1.0}_{-0.8}$	$847.0^{+23.3}_{-5.3}$	$0.9700^{+0.0002}_{-0.0013}$	$8.96^{+1.82}_{-2.12}$	$1668.5^{+44.8}_{-10.2}$	$-0.049^{+0.035}_{-0.032}$	279^{+11}_{-10}	$15.7^{+1.0}_{-1.0}$
2014/12/12	$25.33^{+1.82}_{-0.36}$	$3.4^{+0.9}_{-0.7}$	$30.3^{+2.9}_{-4.8}$	$847.0^{+23.3}_{-5.3}$	$0.9700^{+0.0002}_{-0.0013}$	$8.96^{+1.82}_{-2.12}$	$1668.5^{+44.8}_{-10.2}$	$-0.049^{+0.035}_{-0.032}$	279^{+11}_{-10}	$16.9^{+1.5}_{-1.9}$
2014/12/14	$25.33^{+1.82}_{-0.36}$	$2.4^{+0.4}_{-0.3}$	$27.8^{+1.2}_{-1.0}$	$847.0^{+23.3}_{-5.3}$	$0.9700^{+0.0002}_{-0.0013}$	$8.96^{+1.82}_{-2.12}$	$1668.5^{+44.8}_{-10.2}$	$-0.049^{+0.035}_{-0.032}$	279^{+11}_{-10}	$12.9^{+0.9}_{-0.9}$
2014/12/15	$25.33^{+1.82}_{-0.36}$	$2.8^{+0.5}_{-0.4}$	$27.5^{+2.4}_{-1.5}$	$847.0^{+23.3}_{-5.3}$	$0.9700^{+0.0002}_{-0.0013}$	$8.96^{+1.82}_{-2.12}$	$1668.5^{+44.8}_{-10.2}$	$-0.049^{+0.035}_{-0.032}$	279^{+11}_{-10}	$13.6^{+1.3}_{-1.2}$
2014/12/19	$25.33^{+1.82}_{-0.36}$	$2.5^{+0.2}_{-0.2}$	$28.7^{+1.2}_{-0.9}$	$847.0^{+23.3}_{-5.3}$	$0.9700^{+0.0002}_{-0.0013}$	$8.96^{+1.82}_{-2.12}$	$1668.5^{+44.8}_{-10.2}$	$-0.049^{+0.035}_{-0.032}$	279^{+11}_{-10}	$14.1^{+1.0}_{-1.0}$
2015/01/03	$25.33^{+1.82}_{-0.36}$	$2.2^{+0.2}_{-0.2}$	$19.0^{+0.6}_{-0.5}$	$847.0^{+23.3}_{-5.3}$	$0.9700^{+0.0002}_{-0.0013}$	$8.96^{+1.82}_{-2.12}$	$1668.5^{+44.8}_{-10.2}$	$-0.049^{+0.035}_{-0.032}$	279^{+11}_{-10}	$10.7^{+0.6}_{-0.6}$
2015/01/20	$25.33^{+1.82}_{-0.36}$	$2.6^{+0.3}_{-0.2}$	$14.8^{+0.3}_{-0.5}$	$847.0^{+23.3}_{-5.3}$	$0.9700^{+0.0002}_{-0.0013}$	$8.96^{+1.82}_{-2.12}$	$1668.5^{+44.8}_{-10.2}$	$-0.049^{+0.035}_{-0.032}$	279^{+11}_{-10}	$8.0^{+0.4}_{-0.4}$
2015/02/15	$25.33^{+1.82}_{-0.36}$	$2.0^{+0.3}_{-0.3}$	$14.8^{+0.3}_{-0.7}$	$847.0^{+23.3}_{-5.3}$	$0.9700^{+0.0002}_{-0.0013}$	$8.96^{+1.82}_{-2.12}$	$1668.5^{+44.8}_{-10.2}$	$-0.049^{+0.035}_{-0.032}$	279^{+11}_{-10}	$5.5^{+0.3}_{-0.3}$
2015/04/17	$25.33^{+1.82}_{-0.36}$	$20.1^{+3.8}_{-3.0}$	$13.9^{+0.5}_{-1.2}$	$847.0^{+23.3}_{-5.3}$	$0.9700^{+0.0002}_{-0.0013}$	$8.96^{+1.82}_{-2.12}$	$1668.5^{+44.8}_{-10.2}$	$-0.049^{+0.035}_{-0.032}$	279^{+11}_{-10}	$3.0^{+0.3}_{-0.2}$

Note. – The associated uncertainties at 90% confidence level are calculated with the MCMC method. Cols (1)–(11): Date: observational time (year/month/day); r_p : orbital pericenter of star; ϕ_d : disk-pericenter orientation with respect to the LOS projected in the disk plane; i_d : inclination angle of the disk rotation axis with respect to the LOS; a_d : disk semimajor; e_d : disk eccentricity; r_1 ($r_1 = \xi_1 r_S$): inner radius of the emission line regions; r_{br} : radial extent of the coronal X-ray sources; α_1 : emissivity power-law index of inner disk regions; σ : local velocity dispersion of emission line.; ϵ_0 ($10^{28} \text{ erg s}^{-1} \text{ cm}^{-2} \text{ \AA}^{-1} \text{ sr}^{-1}$): constant of the reflection optical line emissivity of the accretion disk.

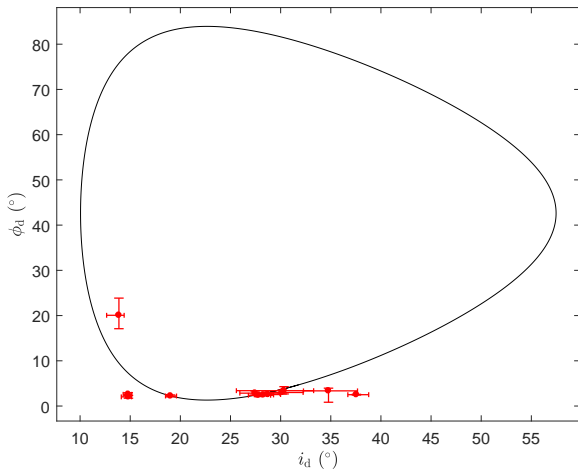


Figure 8. The relation between the disk azimuthal angle ϕ_d and inclination i_d (filled circle), consistent with the clockwise precession of an elliptical accretion disk (solid). The rotation axis of the elliptical accretion disk misaligns by about 23.7° with the spin axis of BH, which inclines with respect to the LOS by about 33.8° . The associated uncertainties at 90% confidence level calculated with MCMC are plotted.

The time dependence of the disk inclination and pericenter azimuthal position angles is consistent with the precession of the elliptical accretion disk with period $T_{LS} \approx 954$ days, about 7 times longer than the duration of the spectral observational campaign. The accretion disk in ASASSN-14li is nearly face-on with an inclination angle i_d from about 38° to 14° with respect to the LOS, which is much smaller than the inclination angle $i_d \approx 88^\circ$ in the TDE candidate PTF09djl (Liu et al. 2017). The viewing angle effects must be significant in PTF09djl but small in ASASSN-14li. Because the He emission lines are produced in a region of ionized accretion disk with electron scattering optical depth (τ_{es}) a few times larger than that for H lines (Roth et al. 2016), He emission lines are expected to be strong in the optical spectra of TDEs with face-on accretion disk. Because the effective optical depth τ_{eff} changes with disc incli-

nation angle, $\tau_{eff} = \tau_{es}/\cos(i_d)$, the escaped line photons are from shallower layers with the increase of disk inclination angle, and consequently both the He and H emission lines are attenuated. However, He line photons are produced in deeper layers with larger τ_{es} and higher temperature than that of H line photons, so the attenuation of He lines is much more significant. The viewing angle effect of the large disk inclination $i_d \approx 88^\circ$ would lead to the weakness/absence of He emission lines in the optical spectra of the TDE candidate PTF09djl, while the disk inclination angle i_d decreasing from about 38° to about 14° is consistent with the prominent detection of the He emission lines with the increasing enhanced intensities relative to the H emission lines in the optical spectra of ASASSN-14li, as reported by Hung et al. (2017). This is consistent with the scenario suggested by Liu et al. (2017) that the diversities of the relative intensity of He and H emission lines in the spectra of the optical/UV TDEs and candidates are due to different disk inclinations.

For an eccentricity $e = 0.9700$, Equation (15) gives a conversion efficiency of $\eta \approx 3.69 \times 10^{-3}$ before the stellar debris passing the marginal stable orbit about $2r_S$ falls freely onto the BH, consistent with the suggestion of low efficiency in TDEs (Svirski et al. 2017). For a stellar tidal disruption by SMBH of mass $M_{BH} \approx 10^{6.23} M_\odot$ with $\beta \sim 1$, the fallback stellar debris mass rate has a peak $\dot{M}_p \sim A_{5/3} (M_{BH}/10^6 M_\odot)^{-1/2} M_\odot \text{ yr}^{-1} \sim 1.02 M_\odot \text{ yr}^{-1}$ with $A_{5/3} \approx 1.33$ (Guillochon & Ramirez-Ruiz 2013), which gives a total peak luminosity $L_p \approx \eta \dot{M}_p c^2 \sim 2.1 \times 10^{44} \text{ erg s}^{-1}$. Because the Eddington luminosity for mass $M_{BH} = 10^{6.23} M_\odot$ is $L_{Edd} \approx 2.1 \times 10^{44} \text{ erg s}^{-1}$, we have $L_p \sim L_{Edd}$. The peak accretion of the TDE ASASSN-14li radiates at about the Eddington limit. ASASSN-14li has been detected in X-rays (Miller et al. 2015; Holoien et al. 2016a; van Velzen et al. 2016; Kara et al. 2017), optical/UV (Holoien et al. 2016a; Brown et al. 2017), infrared (Jiang et al. 2016), and radio (van Velzen et al. 2016; Alexander et al. 2016). The integrated peak optical/UV and X-ray luminosities are $L_{opt} \sim 6.1 \times 10^{43} \text{ erg s}^{-1}$ (Holoien et al. 2016a) and $L_X \sim 3 \times 10^{43} \text{ erg s}^{-1}$ in the range 0.3–10 keV (Miller et al. 2015; Holoien et al. 2016a; van Velzen et al. 2016; Kara et al. 2017), respectively. The energy output of ASASSN-14li

is dominated in the X-ray and optical/UV bands and has a peak bolometric luminosity $L_{\text{bol}} \sim L_{\text{opt}} + L_X \sim 0.9 \times 10^{44} \text{ erg s}^{-1}$, consistent with the expected maximum luminosity L_p .

It is not very clear how TDEs excite the strong optical and UV emission lines. In the accretion disk model for the broad optical emission lines, there are three possible energy sources: (1) a radially extended hot corona above the accretion disk surfaces, (2) the interaction shocks at nearly the apogee of the accretion disk (Piran et al. 2015), and (3) the compressing shocks at the pericenter of the accretion disk. We have modeled the line emissivity with a broken power-law in radius. If the shocks at about the apogee of the accretion disk are the driving sources of emission lines, the break radius r_{br} should be about the locations of the shocks at near the disk apogee and the line emissivity α_1 is negative (Wilkins & Fabian 2012; Gonzalez et al. 2017). The compressing shocks at the disk pericenter may heat the accretion disk to radiate soft X-rays (Piran et al. 2015; Krolik et al. 2016), and the hot materials may emit optical emission lines by recombinations when they move out radially and cool down. If the compressing shocks at the disk pericenter are the driving energy sources of the emission lines, the line emissivity would have a single power-law in radius, and the radius r_{br} would be at about the disk radius at which the disk central temperature drops below the Hydrogen recombination temperature. The emission lines are most probably powered by extended coronal X-ray sources, and the broken radius r_{br} is the radial extent of the coronal X-ray sources. The coronal X-ray source is powered by local dissipation of magnetic flux due to the reconnection of the magnetic field lines anchoring the ionized accretion disk underneath. In circular accretion disk, the toroidal magnetic fields may be generated by magneto-rotational instability (MRI) and are amplified by differential rotation. The magnetic flux is proportional to the local orbital shear Ω with Ω the orbital angular frequencies. The magnetic field rises out of the disk surface due to Parker instability and dissipates locally because of the reconnection of magnetic field loops (Field & Rogers 1993; Pariev et al. 2003; Parkin 2014; Begelman et al. 2015). The MRI turbulence regenerates the magnetic fields on a dynamical timescale (Balbus & Hawley 1991). The dissipation of magnetic flux powers the emission lines, probably leading to a power-law radial distribution of H α line emissivity in stars and cataclysmic variables with circular accretion disk (Horne & Saar 1991). It is unclear what kind of radial configuration the magnetic flux has in an extremely eccentric accretion disk. The power-law index $\alpha_1 = -0.049$ in the TDE ASASSN-14li is consistent with a flat coronal X-ray source.

For an ionized optically thick accretion disk irradiated by X-rays, the reflected spectra have prominent optical emission lines, when the ionization parameter is in the range $1 \leq \zeta (\text{erg cm s}^{-1}) \lesssim 500$ (García et al. 2013), where $\zeta = 4\pi F_x/n_e$ with F_x the integrated flux in the energy range 0.1 – 300 keV and n_e the electron number density. From Equation (15), the accretion disk of semimajor $a_d \approx 847.0 r_S$ and eccentricity $e_d \approx 0.970$ has a typical peak temperature $T_p \approx 3 \times 10^4 \text{ K}$. The elliptical accretion disc of ASASSN-14li is ionized. The X-ray spectra of ASASSN-14li are soft (Miller et al. 2015; Holoien et al. 2016a; van Velzen et al. 2016; Kara et al. 2017). Provided that about ten percent the X-ray luminosity $L_x \approx 3 \times 10^{43} \text{ ergs s}^{-1}$ in the 0.3–10 keV range (Holoien et al. 2016a) or one percent of the extrapolated X-ray luminosity $L_x \approx 3.2 \times 10^{44} \text{ ergs s}^{-1}$ in the 0.1–10 keV range (Miller et al. 2015) is from an extended coronal X-ray source, the ionization parameter of ASASSN-14li is $\zeta \sim 6\pi L_x (m_p/1.2M_*) (1 + e_d) a_d (H/r) [1 + (H/r)^2]^{-1} \approx 3.3 \text{ erg cm s}^{-1}$ for $M_* \sim M_\odot$ and disk opening angle $H/r \sim 0.1$, where m_p is the

mass of proton and the typical disk mass at peak $M_d \sim M_*/3$ is assumed.

The fits to the weak wings of the emission lines can be slightly improved if a bulk velocity $v_m \sim -1100 \text{ km s}^{-1}$ is included in the modeling. Because the wings of the broad emission lines are noisy, the constraint on the bulk velocity is very weak. Recent investigations show that the thickness of a circular accretion disk can modify the wings and shift the peak of the line profiles due to the self-shadowing of the accretion disk and to the irradiation of the central ‘eye wall’ of the inner disk (Taylor & Reynolds 2018). The fitting to the wings and peak of the line profiles with a thin accretion disk model would result in some biases in estimates of the parameters of the system, in particular the disk position angle ϕ_d and inclination i_d . It is unclear what are the effects of the height of an extremely eccentric accretion disk on the model line profiles. To fully understand the effects of the disk height on the line profiles and estimates of the disk parameters, a more elaborated elliptical accretion disk model and observed spectra of high signal-to-noise ratio are needed.

In conclusion, we have successfully modeled the complex and asymmetric H α profiles of the TDE ASASSN-14li with a relativistic elliptical disk model. The accretion disk in ASASSN-14li has a large semimajor axis and extreme eccentricity and is probably covered by a largely extended coronal X-ray source of power-law radial distribution. The coronal X-ray sources in TDEs have very different structures from those in active galactic nuclei (AGNs) or Galactic X-ray binaries, which are compact. Our results show that modelling the complex optical line profiles is powerful in probing the structures of the accretion disk and coronal X-ray sources.

ACKNOWLEDGEMENTS

We are grateful to Jose Luis Prieto and Subo Dong for kindly providing us the electronic data of the spectra. This work is supported by the National Natural Science Foundation of China (NSFC11473003) and the Strategic Priority Research Program of the Chinese Academy of Sciences (Grant No. XDB23010200 and No. XDB23040000). LCH was supported by the National Key R&D Program of China (2016YFA0400702) and the National Science Foundation of China (11473002, 11721303).

REFERENCES

- Abramowicz, M., Jaroszynski, M., & Sikora, M. 1978, *A&A*, 63, 221
- Ahn, C.P., Alexandroff, R., Allende Prieto, C., et al. 2012, *ApJS*, 203, 21
- Alexander, K.D., Berger, E., Guillochon, J., et al. 2016, *ApJ*, 819, L25
- Arcavi, I., Gal-Yam, A., Sullivan, M., et al. 2014, *ApJ*, 793, 38
- Balbus, S.A., & Hawley, J.F. 1991, *ApJ*, 376, 214
- Beckwith, K., Armitage, P.J., & Simon, J.B. 2011, *MNRAS*, 416, 361
- Begelman, M.C., Armitage, P.J., & Reynolds, C. S. 2015, *ApJ*, 809, 118
- Beloborodov, A.M. 2002, *ApJ*, 566, L85
- Bogdanović, T., Roseanne, R.M., & Amaro-Seoane, P. 2014, *ApJ*, 788, 99
- Bonnerot, C., Rossi, E. M., & Lodato, G., 2017, *MNRAS*, 464, 2816
- Bonnerot, C., Rossi, E. M., Lodato, G., & Price, D. J. 2016, *MNRAS*, 455, 2253
- Brown, J. S., Holoien, T.W.-S., Auchettl, K., et al. 2017, *MNRAS*, 466, 4904
- Cardelli, J. A., Clayton, G. C., & Mathis, J. S. 1989, *ApJ*, 345, 245
- Carr, J.S., Tokunaga, A.T., & Najita, J. 2004, *ApJ*, 603, 213
- Centko, S.B., Cucchiara, A., Roth, N., et al. 2016, *ApJ*, 818, L32
- Chen, K., Halpern, J.P., & Filippenko, A.V. 1989, *ApJ*, 339, 742
- Dai, L., McKinney, J.C., & Miller, M.C. 2015, *ApJ*, 812, L39
- De Falco, V., Falanga, M., & Stella, L. 2016, *A&A*, 595, A38

- Eracleous, M., Livio, M., Halpern, J.P., & Storchi-Bergmann, T. 1995, *ApJ*, 438, 610
- Evans, C.R., & Kochanek, C.S. 1989, *ApJ*, 346, L13
- Field, G.B., & Rogers, R. D. 1993, *ApJ*, 403, 94
- Frank, J., & Rees, M.J. 1976, *mnras*, 176, 633
- French, K.D., Arcavi, I., & Zabludoff, A. 2016, *ApJ*, 818, L21
- García, J., Dauser, T., Reynolds, C.S., et al. 2013, *ApJ*, 768, 146
- Gaskell, C.M., & Rojas Lobos, P.A. 2014, *MNRAS*, 438, L36
- Gezari, S., Chornock, R., Lawrence, A., et al. 2015, *ApJ*, 815, L5
- Gezari, S., Chornock, R., Rest, A., et al. 2012, *Nature*, 485, 217
- Gezari, S., Martin, D.C., Milliard, B., et al. 2006, *ApJ*, 653, L25
- Gonzalez, A.G., et al. 2017, *MNRAS*, 472, 1932
- Guillochon, J. & McCourt, M. 2017, *ApJ*, 834, L19
- Guillochon, J. & Ramirez-Ruiz, E. 2013, *ApJ*, 767, 25
- Guillochon, J., Manukian, H., & Ramirez-Ruiz, E. 2014, *ApJ*, 783, 23
- Hayasaki, K. & Loeb, A. 2016, *Nature Scientific Reports*, 6, 35629
- Hayasaki, K., Stone, N., & Loeb, A. 2013, *MNRAS*, 434, 909
- Hills, J.G. 1975, *Nature*, 254, 295
- Holoien, T.W.-S., Kochanek, C.S., Prieto, J.L., et al. 2016a, *MNRAS*, 455, 2918
- Holoien, T.W.-S., Kochanek, C.S., Prieto, J.L., et al. 2016b, *MNRAS*, 463, 3813
- Holoien, T.W.-S., Prieto, J.L., Bersier, D., et al. 2014, *MNRAS*, 445, 3263
- Horne, K. & Saar, S.H. 1991, *ApJ*, 374, L55
- Horne, K., Marsh, T.R., Cheng, F.H., et al. 1994, *ApJ*, 426, 294
- Hryniewicz, K., & Walter, R. 2016, *A&A*, 586, A9
- Hung, T., Gezari, S., Blagorodnova, N., et al. 2017, *ApJ*, 842, 29
- Jiang, N., Dou, L., Wang, T., et al. 2016, *ApJ*, 828, L14
- Kara, E., Dai, L., Reynolds, C.S., & Kallman, T. 2017, *arXiv:1711.06090*
- Kippenhahn, R., & Weigert, A. 1994, *Stellar Structure and Evolution* (Springer-Verlag Berlin Heidelberg New York.)
- Kochanek, C.S. 1994, *ApJ*, 422, 508
- Kochanek, C. S. 2016, *MNRAS*, 458, 127
- Komossa, S. 2015, *Journal of High Energy Astrophysics*, 7, 148
- Komossa, S. & Bade, N. 1999, *A&A*, 343, 775
- Komossa, S., & Zensus, J.A. 2016, *IAU Symp.* 312, 13
- Komossa, S., Zhou, H., Wang, T., et al. 2008, *ApJ*, 678, L13
- Krolik, J., Piran, T., Svirski, G., & Cheng, R.M. 2016, *ApJ*, 827, 127
- Liu, F.K., Li, S., & Chen, X. 2009, *ApJ*, 706, L133
- Liu, F.K., Li, S., & Komossa, S. 2014, *ApJ*, 786, 103
- Liu, F.K., Zhou, Z.Q., Cao, R., Ho, L.C., & Komossa, S. 2017, *MNRAS*, 472, L99
- Lodato, G., King, A.R., & Pringle, J. E. 2009, *MNRAS*, 392, 332
- Lousto C.O., Zlochower Y., 2011, *Phys. Rev. Lett.*, 1102
- Marsh, T.R., & Dhillon, V.S. 1997, *MNRAS*, 292, 385
- Metzger, B.D., & Stone, N.C. 2016, *MNRAS*, 461, 948
- Miller, J.M., Kaastra, J.S., Miller, M.C., et al. 2015, *Nature*, 526, 542
- Mockler, B., Guillochon, J., & Ramirez-Ruiz, E. 2018, *arXiv:1801.08221*
- Pariev, V.I., Blackman, E.G., & Boldyrev, S.A. 2003, *A&A*, 407, 403
- Parkin, E.R. 2014, *MNRAS*, 438, 2513
- Piran, T., Svirski, G., Krolik, J., Cheng, R. M., & Shiokawa, H. 2015, *ApJ*, 806, 164
- Rees, M.J. 1988, *Nature*, 333, 523
- Ricarte, A., Natarajan, P., Dai, L., & Coppi, P. 2016, *MNRAS*, 458, 1712
- Romero-Canizales, C., Prieto, J.L., Chen, X., et al. 2016, *ApJ*, 832, L10
- Rosswog, S., Ramirez-Ruiz, E., & Hix, W.R. 2009, *ApJ*, 695, 404
- Roth, N., Kasen, D., Guillochon, J., & Ramirez-Ruiz, E. 2016, *ApJ*, 827, 3
- Sadowski, A., Tejeda, E., Gafton, E., et al. 2016, *MNRAS*, 458, 4250
- Schlafly, E. F., & Finkbeiner, D. P. 2011, *ApJ*, 737, 103
- Shiokawa, H., Krolik, J.H., Cheng, R.M., Piran, T., & Noble, S.C. 2015, *ApJ*, 804, 85
- Simon, J.B., Armitage, P.J., & Beckwith, K. 2011, *ApJ*, 743, 17
- Stone, N. & Metzger, B.D. 2016, *MNRAS*, 455, 859
- Strateva, I.V., Strauss, M.A., Hao, L., et al. 2003, *AJ*, 126, 1720
- Strubbe, L.E., & Murray, N. 2015, *MNRAS*, 454, 2321
- Svirski, G., Piran, T., & Krolik, J. 2017, *MNRAS*, 467, 1426
- Taylor, C., & Reynolds, C.S. 2018, *ApJ*, 855, 120
- Tejeda, E., & Rosswog, S. 2013, *MNRAS*, 433, 1930
- van Velzen, S., Anderson, G.E., Stone, N.C., et al. 2016, *Science*, 351, 62
- van Velzen, S., Farrar, G.R., Gezari, S., et al. 2011, *ApJ*, 741, 73
- Wang, T.-G., Zhou, H.-Y., Komossa, S., et al. 2012, *ApJ*, 749, 115
- Wevers, T., van Velzen, S., Jonker, P.G., et al. 2017, *MNRAS*, 471, 1694
- Wilkins, D.R., & Fabian, A.C. 2012, *MNRAS*, 424, 1284
- Zabludoff, A.I., et al. 1996, *ApJ*, 466, 104

This paper has been typeset from a $\text{\TeX}/\text{\LaTeX}$ file prepared by the author.